

Continuous-Time Line-of-Sight Constrained Trajectory Planning for 6-Degree of Freedom Systems

Christopher R. Hayner¹, John M. Carson III², Behçet Açıkmeşe¹, and Karen Leung¹

Abstract— Perception algorithms are ubiquitous in modern autonomy stacks, providing necessary environmental information to operate in the real world. Many of these algorithms depend on the visibility of keypoints, which must remain within the robot’s line-of-sight (LoS), for reliable operation. This paper tackles the challenge of maintaining LoS on such keypoints during robot movement. We propose a novel method that addresses these issues by ensuring applicability to various sensor footprints, adaptability to arbitrary nonlinear dynamics, and constant enforcement of LoS throughout the robot’s path. Through our experiments, we show that the proposed approach achieves significantly reduced LoS violation and runtime compared to existing state-of-the-art methods in several representative and challenging scenarios.

I. INTRODUCTION

Perception algorithms are essential for enabling robots to perform relative navigation and tracking tasks, allowing them to gather information about internal and external states (*e.g.*, pose estimation, obstacle avoidance) without relying on external sources (*e.g.*, GNSS, motion capture, cooperative agents). Given the increasing interest in deploying robotics in real-world unknown environments, there is a heavy reliance on perception algorithms for the aforementioned *safety critical* tasks, perception algorithms must be reliable. A central requirement for these algorithms, which depend on observing keypoints or points-of-interest, is that these keypoints must always remain visible to the robot. For example, landmarks within visual-inertial odometry, [1], [2], a subject being filmed in a drone-enabled cinematography application, [3], [4], or prospective landing sites and hazards for a planetary lander, [5], [6], [7]. If keypoints do not remain visible while the robot is moving, perception performance may suffer likely resulting in the task being considered a failure. In this paper, we consider the problem of trajectory optimization with LoS constraints as *LoS guidance*.

¹ Dept. of Aeronautics and Astronautics, University of Washington, Seattle, WA, USA. Email: haynec@uw.edu

² NASA Johnson Space Center, Houston, TX, USA

This work was supported by a NASA Space Technology Graduate Research Opportunity and the Office of Naval Research under grant N00014-17-1-2433.

The authors would like to acknowledge Natalia Pavlasek, Griffin Norris, Samuel Buckner, and Purnanand Elango for their many helpful discussions and support throughout this work.

The code and implementation details for this work can be found <https://haynec.github.io/papers/los>.

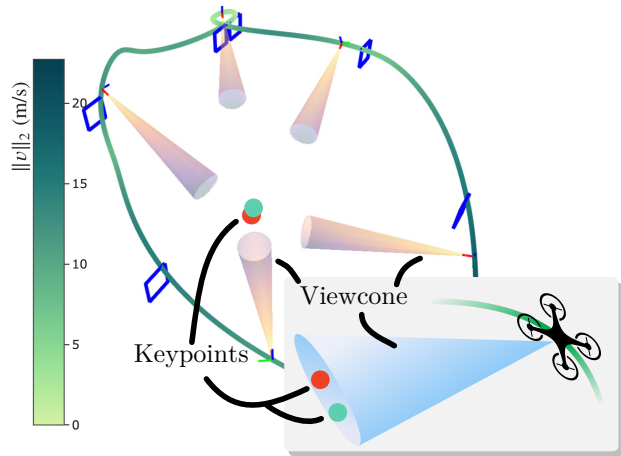


Fig. 1: LoS Guidance: A simulation result of our LoS guidance method showing the pose of the quadrotor and view cone at several points along the trajectory. Throughout the trajectory, the two key points are within the LoS.

State-of-the-art methods for LoS guidance in these applications suffer from several limitations: they lack generality to different sensor footprints (*e.g.* cameras, LiDARs), are not adaptable to arbitrary nonlinear dynamics, and only enforce LoS at discrete points along the trajectory. We present a method of LoS guidance that addresses the key requirements for an effective, realizable, and generalizable LoS guidance method:

- R1.** applicability to different sensor footprints,
- R2.** adaptability to arbitrary nonlinear dynamics, and
- R3.** maintain LoS on keypoints throughout the entire trajectory.

Contributions. The contributions of this paper are three-fold: **1.** a sensor footprint agnostic line-of-sight constraint, **2.** a computationally tractable formulation of a continuous-time line-of-sight guidance methodology, CT-LoS, as well as a baseline discrete-time line-of-sight DT-LoS guidance methodology, and finally **3.** a demonstration of the efficacy of CT-LoS and a comparison against DT-LoS in several keypoint tracking problems inspired by challenges encountered in relative navigation and drone-enabled cinematography.

Organization. This paper is organized into the following sections. Section II discusses related work in the field. Section III introduces the general problem as well as the notation used throughout this paper. Section IV

introduces the rigid body dynamics and six degree of freedom line-of-sight constraint. CT-LoS is introduced as the solution method in Section V. The experiments and baseline comparison are introduced in Section VI. Results from these experiments are discussed in Section VII. Finally, conclusions are discussed in Section VIII. **Terminology:** We use the term *six degree of freedom* when referring to the three translational modes and three rotational modes of a rigid body.

II. LITERATURE REVIEW

In this section, we offer a brief taxonomy of nonlinear trajectory optimization techniques with LoS constraints, seen in Table I, and justification for our formulation and methodology.

Method	R1	R2	R3
[8], [9], [10], [11]	✗	✗	✗
[12], [13]	✗	✓	✗
Baseline	✓	✓	✗
Proposed	✓	✓	✓

TABLE I: Classification of Related Work

Pseudospectral trajectory planning, as discussed in Section 9.7 [14], is a method that parameterizes state and control profiles using polynomial splines, with coefficients or knot points as decision variables in the NLP. For quadrotors, these methods often use the differentially flat model from [15], optimizing position and yaw angle trajectories either independently or jointly. They are effective for generating online trajectories [16], [17].

For LoS guidance, [8] proposed a pseudospectral method following a two-step decoupled approach, maximizing information gain by adjusting yaw angles to include the regions in LoS with the highest uncertainty. However, this method does not strictly constrain points of interest to be within the sensor’s LoS. Similarly, [10] and [11] use a decoupled approach but enforce a symmetric second-order cone constraint to keep keypoints within the LoS. However, the decoupled approach results in greedy solutions as positions are optimized without considering LoS constraints. To address this, [9] jointly optimize position and yaw angle. This allows for overall less conservative solutions when compared to the decoupled approach. However, as these are pseudospectral methods, dynamic feasibility is limited to convex min-max constraints on the flat states and their derivatives, and cannot be generalized to arbitrary nonlinear dynamics.

In contrast to pseudospectral methods, [12] adopts a multiple-shooting method (see Section 9.6 in [14]) and directly imposes the nonlinear quadrotor dynamics constraint with no assumption of differential flatness at each discrete node. However, keypoint inclusion in LoS, modeled by a non-symmetric L_∞ -norm cone, is only promoted in the cost function rather than directly enforced as a constraint. Thus resulting in insufficient satisfaction of LoS constraints which cannot generalize to other sensor types.

All of the aforementioned methods leverage software such as ACADO [18] and NLOPT [19] to solve the NLP. These packages call underlying NLP solvers such as IPOPT [20] or convex approximation algorithms such as sequential quadratic programming [21]. A limitation of relying on these solvers is they lack convergence guarantees, rely on second-order information, and they cannot enforce constraints in continuous-time. In contrast, successive convexification-based methods (SCvx) has gained significant popularity in trajectory optimization, [22], [23], as they have convergence guarantees [24], only require first-order information¹, and, recently, have guarantees on continuous-time constraint satisfaction [26]. SCP has been used to solve the LoS guidance problem in a planetary landing context [13], a symmetric norm cone constraint is enforced at each discrete node to ensure a single landing site is within LoS.

However, these methods only consider a single keypoint and do not generalize to different sensor footprints. Finally, a major limitation of all the LoS guidance methods discussed in this section is that they only enforce the LoS constraint at discrete nodes along the trajectory, rather than in continuous-time. Meaning they lack constraint satisfaction in between nodes, rendering them hazardous in safety-critical situations.

III. GENERAL PROBLEM FORMULATION

In this section, we introduce the notation used throughout the paper in Section III-A and the general continuous-time LoS guidance problem formulation in Section III-B.

A. Notation

We use the following notation in the remainder of this paper. A quantity expressed in the frame \mathcal{A} is denoted by the subscript $\square_{\mathcal{A}}$. The transform from frame \mathcal{A} to frame \mathcal{B} is denoted by the subscript $\square_{\mathcal{A} \rightarrow \mathcal{B}}$. To parameterize the attitude of \mathcal{B} with respect to \mathcal{A} , the unit quaternion, $q_{\mathcal{A} \rightarrow \mathcal{B}} \in \mathcal{S}^3$ where $\mathcal{S}^3 \subset \mathbb{R}^4$ is the unit 3-sphere, is used. The scalar-first convention is used for unit quaternion as follows $q = [q_w \ q_x \ q_y \ q_z]^\top$.

B. Continuous-Time Formulation

We consider a keypoint to be in the LoS of an exteroceptive sensor if it resides within a view cone, as seen in Fig 2. We frame the LoS guidance problem as a general, continuous, free-final time trajectory planning problem (1).

General LoS Problem

$$\underset{x, u, t_f}{\text{minimize}} \quad L_f(t_f, x(t_f), u(t_f)), \quad (1a)$$

$$\text{subject to} \quad \dot{x}(t) = f(t, x(t), u(t)), \quad (1b)$$

$$p(t) \in \mathcal{K}(b(x(t)), c(x(t)), A^C(t)), \quad (1c)$$

$$g(t, x(t), u(t)) \leq 0_{n_g}, \quad (1d)$$

$$h(t, x(t), u(t)) = 0_{n_h}, \quad (1e)$$

$$x(t_i) = x_i, x(t_f) = x_f, \quad (1f)$$

where appropriate, $\forall t \in [t_i, t_f]$.

¹when using a first-order solver, such as [25]

Where $L : \mathbb{R}_+ \times \mathbb{R}^{n_x} \times \mathbb{R}^{n_u} \mapsto \mathbb{R}$ denotes a general state, control and time dependent cost, $f : \mathbb{R}_+ \times \mathbb{R}^{n_x} \times \mathbb{R}^{n_u} \mapsto \mathbb{R}^n$ denotes the system dynamics, the set

$$\mathcal{K}(b, c, A^{\text{Cone}}) = \{a \in \mathbb{R}^n \mid \|A^{\text{C}}(a - b)\| \leq c^\top(a - b)\},$$

where $A^{\text{C}} : \mathbb{R}^{n \times n} \mapsto \mathbb{R}^{n \times n}$, $b \in \mathbb{R}^n$, $c \in \mathbb{R}^n$, denotes the view cone. Here a point to be kept within LoS is denoted by a , the position of the sensor is denoted by $b(t)$, the boresight vector is denoted by $c(t)$, and the angular frame of view is denoted by $A^{\text{C}}(t)$ (for the remainder of this paper, the boresight vector and angular frame of view are kept constant). The path constraint functions $g : \mathbb{R}_+ \times \mathbb{R}^{n_x} \times \mathbb{R}^{n_u} \mapsto \mathbb{R}^{n_g}$ denotes general inequality constraints, $h : \mathbb{R}_+ \times \mathbb{R}^{n_x} \times \mathbb{R}^{n_u} \mapsto \mathbb{R}^{n_h}$ denotes general equality constraints, and finally x_i and x_f denote initial and terminal state constraints. We make no assumptions on the convexity of Prob. 1, nor are there assumptions of differential flatness on the dynamics in (1b).

IV. SIX DEGREE OF FREEDOM FORMULATION

This section gives an overview of the six degree of freedom dynamics in Section IV-A and introduces the proposed LoS constraint in Section IV-B.

A. Dynamics

We adopt the six degree of freedom rigid body dynamics similar to those used in [27], [28]. The vehicle state is defined as, $x = [r_{\mathcal{I}}^\top \ v_{\mathcal{I}}^\top \ q_{\mathcal{B} \rightarrow \mathcal{I}}^\top \ \omega_{\mathcal{B}}^\top]^\top$, where the position resolved in the inertial frame is $r_{\mathcal{I}} \in \mathbb{R}^3$, the velocity resolved in the inertial frame is $v_{\mathcal{I}} \in \mathbb{R}^3$, the attitude of the body frame relative to the inertial frame is $q_{\mathcal{B} \rightarrow \mathcal{I}}$, and angular rate of the body frame relative to an inertial frame is $\omega_{\mathcal{B}} \in \mathbb{R}^3$. The vehicle control vector, $u(t) = [f_{\mathcal{B}}^\top \ M_{\mathcal{B}}^\top]^\top$ consists of the thrust vector represented in the body frame, $f_{\mathcal{B}} \in \mathbb{R}^3$ and moment vector $M_{\mathcal{B}} \in \mathbb{R}^3$.

Position. $\dot{r}_{\mathcal{I}}(t) = v_{\mathcal{I}}(t)$

Velocity. $\dot{v}_{\mathcal{I}}(t) = \frac{1}{m} (C(q_{\mathcal{B} \rightarrow \mathcal{I}}(t))f_{\mathcal{B}}(t)) + g_{\mathcal{I}}$

Attitude. $\dot{q}_{\mathcal{I} \rightarrow \mathcal{B}} = \frac{1}{2} \Omega(\omega_{\mathcal{B}}(t))q_{\mathcal{I} \rightarrow \mathcal{B}}(t)$

Angular Rate. $\dot{\omega}_{\mathcal{B}}(t) = J_{\mathcal{B}}^{-1} (M_{\mathcal{B}}(t) - [\omega_{\mathcal{B}}(t) \times] J_{\mathcal{B}} \omega_{\mathcal{B}}(t))$

Where $g_{\mathcal{I}} \in \mathbb{R}^3$ is the gravity of Earth expressed in the inertial reference frame, and $J_{\mathcal{B}}$ is the inertial tensor of the vehicle expressed in the body frame. The operator $C : \mathcal{S}^3 \mapsto SO(3)$ represents the direction cosine matrix (DCM), where $SO(3)$ denotes the special orthogonal group. For a vector $\xi \in \mathbb{R}^3$, the skew-symmetric operators $\Omega(\xi)$ and $[\xi \times]$ are defined in Section II.A. in [29]. Using the aforementioned definitions, the 6-DoF dynamics are

$$f_{\text{6DOF}}(t, x(t), u(t)) = [r_{\mathcal{I}}(t)^\top \ v_{\mathcal{I}}(t)^\top \ q_{\mathcal{I} \rightarrow \mathcal{B}}(t)^\top \ \omega_{\mathcal{B}}(t)^\top]^\top.$$

B. Nonconvex Line-of-Sight Formulation

The line of sight constraint ensures that a set of keypoints remain within a view cone, \mathcal{K} which models an exteroceptive sensor's frame of view. This sensor is assumed to be rigidly attached to the body of the vehicle. As such, both the position and attitude of the sensor are solely determined by the position and attitude of the

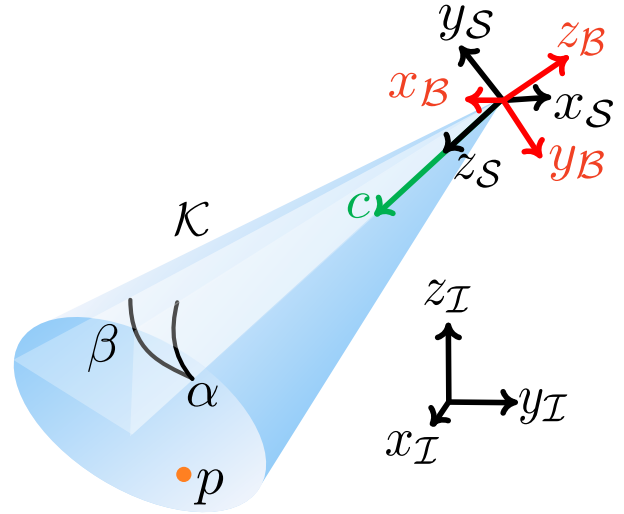


Fig. 2: Norm Cone: The inertial, body, and sensor frames are denoted by the axis with subscripts \mathcal{I} , \mathcal{B} , and \mathcal{S} respectively. The keypoint is shown by the orange point p , the boresight vector, c , of the cone, \mathcal{K} , is represented by the green vector, and the angles of the view cone α and β are visualized on the cone.

vehicle. The line of sight constraint can be broken up into two parts: **1.** a non-convex transformation component that expresses the transform from the inertial frame to the sensor frame and **2.** a convex norm cone component expressed in the sensor frame.

1) *Transformation Component:* Given the location of a keypoint represented in the inertial frame, $p_{\mathcal{I}}(t)$ and the vehicle state, $x(t)$, the sensor frame representation of the keypoint is

$$p_{\mathcal{S}}(t) = C(q_{\mathcal{S} \rightarrow \mathcal{B}})C(q_{\mathcal{B} \rightarrow \mathcal{I}}(t))(p_{\mathcal{I}}(t) - r_{\mathcal{I}}(t)). \quad (2)$$

2) *Norm Cone Component:* Given a keypoint resolved in the sensor frame, $p_{\mathcal{S}}(t)$, the sensor view cone is modeled using a norm cone,

$$\|A^{\text{C}} p_{\mathcal{S}}(t)\|_p \leq c^\top p_{\mathcal{S}}(t). \quad (3)$$

The z -axis of the sensor frame is chosen to be aligned with the boresight vector, c , of the cone, meaning $c = [0 \ 0 \ 1]^\top$. It follows that Σ is defined as

$$A^{\text{C}} \triangleq \begin{bmatrix} \frac{1}{\tan(\alpha)} & 0 & 0 \\ 0 & \frac{1}{\tan(\beta)} & 0 \\ 0 & 0 & 0 \end{bmatrix},$$

where α and β are the angles of the field of view that are aligned with the $x_{\mathcal{S}}$ and $y_{\mathcal{S}}$ axis respectively. The norm cone is visualized in Fig 2. As most exteroceptive sensors have either rectangular or circular frames of view, either $p = \infty$ or $p = 2$ respectively are the appropriate choice of p -norm for (3). However, this method extends to any norm. Notably, (3) is a convex constraint in $p_{\mathcal{S}}(t)$ (see Section 2.2.3 in [30]).

3) *Line of Sight Constraint:* Substituting (2) into (3) yields the full nonconvex line of sight constraint

$$g_{\text{LoS}} \triangleq \|\Sigma C(q_{\mathcal{S} \rightarrow \mathcal{B}})C(q_{\mathcal{B} \rightarrow \mathcal{I}}(t))(p_{\mathcal{I}}(t) - r_{\mathcal{I}}(t))\| - c^\top C(q_{\mathcal{S} \rightarrow \mathcal{B}})C(q_{\mathcal{B} \rightarrow \mathcal{I}}(t))(p_{\mathcal{I}}(t) - r_{\mathcal{I}}(t)) \leq 0, \quad (4)$$

and define it as g_{LoS} for notational brevity. When (4) is satisfied, $p \in \mathcal{K}$.

V. CT-LoS ALGORITHM

Traditional SCvx-based methods solve the continuous-time LoS guidance problem, Prob. 1, by approximating it in discrete-time and enforcing constraints at each discrete node. Choosing a sparse discretization grid can lead to large inter-nodal constraint violations while increasing nodes increases the computational costs. The CT-SCvx algorithm by [26] solves the problem directly by integrating constraints over the entire trajectory, avoiding this approximation. In this section, we will present a brief problem-specific overview of the constraint reformulation, time dilation, control parameterization, linearization, discretization, and convex subproblem steps of the CT-SCvx method. The overall algorithm is visualized in Fig. 3. A comprehensive overview written in a more general context of the CT-SCvx method can be found in [26].

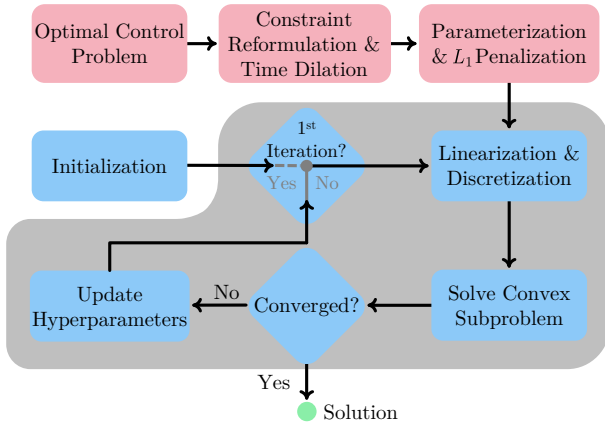


Fig. 3: The CT-SCvx-based CT-LoS algorithmic outline

A. Isoparametric Constraint Reformulation

To ensure continuous-time constraint satisfaction, (4) is reformulated as

$$g_{\text{LoS}}(t, x(t), u(t)) \leq 0 \quad \forall t \in [t_i, t_f] \iff \int_{t_i}^{t_f} \max\{0, g_{\text{LoS}}(t, x(t), u(t))\}^2 dt = 0. \quad (5)$$

To satisfy (4), it is sufficient to satisfy the RHS of (5) which was proposed and proved in Lemma 2 and its proof in [26]. A new state is defined

$$\begin{aligned} \dot{y}(t) &= \max\{0, g_{\text{LoS}}(t, x(t), u(t))\}^2, \\ y(t_i) &= y(t_f). \end{aligned}$$

The new state, $y : \mathbb{R}_+ \mapsto \mathbb{R}$, is concatenated to the original state vector forming a new augmented state vector

$$\tilde{x}(t) = [x(t)^\top \quad y(t)^\top]^\top, \quad (6)$$

and augmented dynamics

$$\dot{\tilde{x}}(t) = \begin{bmatrix} f_{6\text{DOF}}(t, x(t), u(t)) \\ \max\{0, g_{\text{LoS}}(t, x(t), u(t))\}^2 \end{bmatrix}. \quad (7)$$

B. Time Dilation

Time dilation is shown as an effective method to solve free final time problems with a uniform time grid in [29] and with an adaptive time grid in [31]. Time dilation reformulates a free-final time problem as an equivalent fixed-final time problem by shrinking or expanding, hence “dilating”, the time interval and treating the dilation constants, $s \in \mathbb{R}$, as a control input. To allow each discrete node to freely move in the time-domain, we adopt the time dilation with an adaptive time grid. A uniform normalized time grid, $\tau \in [0, 1]$, is introduced and the mapping back to the original time interval is $t(\tau) : [0, 1] \rightarrow [t_i, t_f]$. The time-dilation constant is defined as

$$s(\tau) \triangleq \frac{dt(\tau)}{d\tau} > 0.$$

We treat the time dilation constant, $s(\tau)$, as a control input and define the augmented control vector as

$$\tilde{u}(\tau) = [u(t(\tau))^\top \quad s(\tau)]^\top. \quad (8)$$

We can express (7) in normalized time

$$\begin{aligned} \overset{\circ}{\tilde{x}}(\tau) &= \frac{d\tilde{x}(t(\tau))}{d\tau} \\ &= \frac{d\tilde{x}(t(\tau))}{dt(\tau)} \frac{dt(\tau)}{d\tau} \\ &= s(\tau) \begin{bmatrix} f_{6\text{DOF}}(t(\tau), x(t(\tau)), u(t(\tau))) \\ \dot{y}(t(\tau)) \end{bmatrix} \\ &= F(\tilde{x}(\tau), \tilde{u}(\tau)), \end{aligned} \quad (9)$$

where the derivative with respect to τ is denoted as $\overset{\circ}{\square}$. In the remainder of this paper all controls, u , are the augmented form defined in (8). We omit the tilde operator on the control for notational simplicity.

C. Control Parameterization

We use a first-order hold (FOH) control parameterization as the resulting trajectory and control are smoother and easier to track by real-world vehicles [27]. For discrete control signals, u_k and u_{k+1} , the continuous control signal on the interval $[\tau_k, \tau_{k+1})$ is defined as follows

$$u(\tau) \triangleq \sigma_k^-(\tau)u(k) + \sigma_{k+1}^+(\tau)u(k+1), \quad \forall \tau \in [\tau_k, \tau_{k+1}),$$

where

$$\sigma_k^-(\tau) \triangleq \frac{\tau_{k+1} - \tau}{\tau_{k+1} - \tau_k}, \quad \sigma_{k+1}^+(\tau) \triangleq \frac{\tau - \tau_k}{\tau_{k+1} - \tau_k}.$$

D. Linearization

A byproduct of the continuous-time reformulation method proposed in [26] is the problem is reformulated into a quadratic program. To pose our problem in this form, we need to approximate all nonlinear constraints with a first-order Taylor series approximation about a reference trajectory, (\tilde{x}, \tilde{u}) . The Jacobians of the dynamics

with respect to \tilde{x} and u are

$$\begin{aligned} A(\tau) &\triangleq \nabla_{\tilde{x}} F(\tilde{x}(\tau), \bar{u}(\tau)), \\ B(\tau) &\triangleq \nabla_u F(\tilde{x}(\tau), \bar{u}(\tau)). \end{aligned}$$

The linear time-varying (LTV) continuous-time dynamics are

$$\Delta \dot{\tilde{x}}(\tau) = A(\tau)\Delta \tilde{x}(\tau) + B(\tau)\Delta u(\tau), \quad (10)$$

where $\Delta \square \triangleq \square - \bar{\square}$.

E. Discretization

To make Problem 1 solvable, we discretize it into a finite-dimensional form. To maintain dynamic feasibility and avoid constraint violations between discrete points, we use the inverse-free exact discretization method from [26], applied to the dynamics in (10). This method is exact, as it relies on the integral form of the differential equation (10).

1) *Discretized Dynamics:* The LTV dynamics with a FOH control parametrization are

$$\begin{aligned} \Delta \tilde{x}(\tau) &\approx A(\tau)\Delta \tilde{x}(\tau) + B(\tau)\sigma_k^-(\tau)\Delta u(\tau_k) + \\ &\quad B(\tau)\sigma_k^+(\tau)\Delta u(\tau_{k+1}), \end{aligned} \quad (11)$$

for $\tau \in [\tau_k, \tau_{k+1})$. The unique solution to (11) is given by (12), shown in [22], [32]

$$\begin{aligned} \Delta \tilde{x}(\tau) &= \Phi_k(\tau, \tau_k)\Delta \tilde{x}(\tau_k) + \int_{\tau_k}^{\tau_{k+1}} \Phi_k(\tau, \xi) \\ &\quad \{B(\xi)\sigma_k^-(\tau)\Delta u_k + B(\xi)\sigma_k^+(\tau)\Delta u_{k+1}\} d\xi. \end{aligned} \quad (12)$$

The state transition matrix associated with Equation (12), denoted by $\Phi_k(\tau, \tau_k)$, $\tau \in [\tau_k, \tau_{k+1})$ satisfies the differential equation

$$\dot{\Phi}_k(\tau, \tau_k) = A(\tau)\Phi_k(\tau, \tau_k), \quad \Phi_k(\tau_k, \tau_k) = \mathbf{I}_{n_{\tilde{x}}}.$$

The LTV discretized dynamics are

$$\Delta \tilde{x}_{k+1} = \bar{A}_k \Delta \tilde{x}_k + \bar{B}_k^- \Delta u_k + \bar{B}_k^+ \Delta u_{k+1}, \quad (13a)$$

$$\bar{A}_k \triangleq \Phi_k(\tau_{k+1}, \tau_k), \quad (13b)$$

$$\bar{B}_k^- \triangleq \int_{\tau_k}^{\tau_{k+1}} \Phi_k(\tau_{k+1}, \xi) B(\xi) \sigma_k^-(\xi) d\xi, \quad (13c)$$

$$\bar{B}_k^+ \triangleq \int_{\tau_k}^{\tau_{k+1}} \Phi_k(\tau_{k+1}, \xi) B(\xi) \sigma_k^+(\xi) d\xi. \quad (13d)$$

F. Convex Subproblem

To formulate the convex subproblem, it is necessary to address numerical stability concerns as well as employ a trust region to ensure convergence. For numerical stability, we adopt an affine scaling method on the state and control similar to the method presented in [33]. The scaled variables are denoted by the $\hat{\square}$ operator. A soft trust region is penalized to ensure the solution, (x, u) , does not deviate too far from the reference or previous solution, (\bar{x}, \bar{u}) . Specifically, we use a squared 2-norm, $\|\square - \bar{\square}\|_2^2$, on the state and control which has convergence guarantees, see Section 5 in [34].

1) *Min-Max State and Control Constraints:* To ensure the convergence of Algorithm 1, the state and control sets \mathcal{X}, \mathcal{U} are assumed to be compact [22]. In practice, this is enforced by defining minimum and maximum bounds for each element of the state and control vectors

$$\tilde{x}_{\min}^i \leq \tilde{x}_k^i \leq \tilde{x}_{\max}^i, \quad \forall i \in \{0, n_x\}, \forall k \in \{0, N\}, \quad (14a)$$

$$u_{\min}^i \leq u_k^i \leq u_{\max}^i, \quad \forall i \in \{0, n_u\}, \forall k \in \{0, N\}. \quad (14b)$$

The boundary condition on the augmented state y is relaxed to

$$y_k - y_{k-1} \leq \varepsilon_{\text{LICQ}} \quad \forall k \in \{1, N\},$$

where $\varepsilon_{\text{LICQ}} \geq 0$ is sufficiently small ($\sim 1 \times 10^{-4}$) such that all feasible solutions do not violate the linear independence constraint qualification (LICQ) outlined in Section 3.1 of [26]. The constraints in (14) are enforced using the same continuous-time constraint reformulation method outlined in V-A.

2) *Convex Subproblem Form:* The convex subproblem for CT-LoS is stated in Prob. (15).

CT-LoS Convex Subproblem

$$\underset{\tilde{x}, \tilde{u}}{\text{minimize}} \quad \lambda_{\text{obj}} L_f(\tilde{x}_N, u_N) + \quad (15a)$$

$$\sum_{k=0}^N \lambda_{\text{tr}} \left\| \begin{bmatrix} \hat{\tilde{x}}_k \\ \hat{\tilde{u}}_k \end{bmatrix} - \begin{bmatrix} \bar{\tilde{x}}_k \\ \bar{\tilde{u}}_k \end{bmatrix} \right\|_2^2 + \lambda_{\text{vc}} \|\nu_k\|_1$$

$$\text{subject to} \quad \begin{aligned} \Delta \tilde{x}_k &= \bar{A}_{k-1} \Delta \tilde{x}_{k-1} + \bar{B}_{k-1}^- \Delta u_{k-1} \\ &\quad + \bar{B}_{k-1}^+ \Delta u_k + \nu_{k-1}, \end{aligned} \quad (15b)$$

$$y_k - y_{k-1} \leq \varepsilon_{\text{LICQ}}, \quad (15c)$$

$$\tilde{x}_0 = \tilde{x}_i, \tilde{x}_N = \tilde{x}_f, \quad (15d)$$

where $\forall k \in \{1, \dots, N\}$.

G. Prox-Linear Method

The prox-linear method is outlined in Alg. 1.

Algorithm 1 Prox-Linear Method

Require: $\epsilon_{\text{tr}}, \epsilon_{\text{vc}}, \epsilon_{\text{vb}}, \bar{x}, \bar{u}, k_{\text{max}}$

Initialize $x \neq \bar{x}, u \neq \bar{u}, \xi_{\text{vc}} \neq 0, \xi_{\text{vb}} \neq 0, k = 1$

while $k < k_{\text{max}}$ **and** $G(x, u, \bar{x}, \bar{u}, \xi_{\text{vc}}, \xi_{\text{vb}})$ **do**

$x, u, \xi_{\text{vc}}, \xi_{\text{vb}} \leftarrow$ Solve Convex Subproblem, either (15) or (17), with linearization about \bar{x}, \bar{u}

$\bar{x}, \bar{u} \leftarrow x, u$

$k \leftarrow k + 1$

end while
return x, u

where,

$$\begin{aligned} G(x, u, \bar{x}, \bar{u}, \xi_{\text{vc}}, \xi_{\text{vb}}) &= \left\| \begin{bmatrix} x \\ u \end{bmatrix} - \begin{bmatrix} \bar{x} \\ \bar{u} \end{bmatrix} \right\|_2^2 > \epsilon_{\text{tr}} \\ &\quad \text{or } \|\xi_{\text{vc}}\|_1 > \epsilon_{\text{vc}} \text{ or } \|\xi_{\text{vb}}\|_1 > \epsilon_{\text{vb}}, \end{aligned}$$

is a boolean operator to determine convergence.

The virtual buffer, ξ_{vb} , models linearized nonconvex path

constraint violations at discrete nodes, while the virtual control, ξ_{vc} , models continuous-time dynamic violations. In the CT-LoS formulation, linearized path constraints are appended to the dynamics, eliminating the need for a virtual buffer as these violations are now captured in the virtual control. The convergence criterion for the trust region, virtual control, and virtual buffer is ϵ_{tr} , ϵ_{vc} , and ϵ_{vb} .

VI. EXPERIMENTS

We evaluate our approach on two representative LoS guidance problems and seek to answer the following questions:

- Q1.** How well does CT-LoS satisfy the LoS constraint throughout the entire trajectory compared to the baseline?
- Q2.** What tradeoffs are made to achieve better LoS violation performance?
- Q3.** How does CT-LoS scale as the problem size increase?

To address the above guiding questions, we will use the following metrics to judge the performance of CT-LoS and DT-LoS across both experiments:

- 1) LoS constraint violation over the full trajectory, LoS_{vio} , which is defined as

$$\text{LoS}_{\text{vio}} \triangleq \frac{\sum_{i=0}^{N_{\text{prop}}} \max\{0, g_{\text{LoS}}(x^i, u^i)\}}{N_{\text{prop}}},$$

- 2) the runtime of Alg. 1,
- 3) the original objective cost, which is the total fuel consumption, in the case of the cinematography scenario, or time-of-flight in the relative navigation scenario,
- 4) the number of iterations it takes Alg. 1 to converge.

Furthermore, we systematically vary the discretization grid size, adjusting the problem size and observe how these changes impact the aforementioned metrics. Finally, we sweep through objective weights for each discretization grid size to avoid over-tuning for specific scenarios and ensure the problems are not cherry-picked.

A. Baseline Comparison

We present a baseline comparison to the CT-LoS formulation which enforces LoS constraint violation at discrete nodes rather than integral of LoS constraint violation and refer to it as the DT-LoS formulation. Except for the LoS constraint, the DT-LoS formulation follows the same formulation and solution steps as the SCvx methods presented in [22].

1) *Discrete-Time Constraints:* All nonconvex constraints are linearized

$$L\Box(x_k, u_k) = \Box(\bar{x}_k, \bar{u}_k) + \nabla_x \Box(\bar{x}_k, \bar{u}_k)(x_k - \bar{x}_k) + \nabla_u \Box(\bar{x}_k, \bar{u}_k)(u_k - \bar{u}_k), \quad (16)$$

where $\Box = g$ for inequality path constraints and $\Box = h$ for equality path constraints. All linearized constraints are enforced using a slack variable and all convex constraints are directly enforced at each node.

2) *DT-LoS Convex Subproblem:* The convex subproblem for DT-LoS is stated in Prob. (17).

DT-LoS Convex Subproblem

$$\begin{aligned} \underset{\hat{x}, \hat{u}}{\text{minimize}} \quad & \lambda_{\text{obj}} L_f(x_N, u_N) + \lambda_{vc} \|\nu_k\|_1 + \\ & + \lambda_{vb} \max\{0, \nu_{g_{\text{LoS}}}\} \end{aligned} \quad (17a)$$

$$+ \sum_{k=0}^N \lambda_{tr} \left\| \begin{bmatrix} \hat{x}_k \\ \hat{u}_k \end{bmatrix} - \begin{bmatrix} \bar{x}_k \\ \bar{u}_k \end{bmatrix} \right\|_2^2$$

$$\begin{aligned} \text{subject to} \quad & \Delta x_k = \bar{A}_{k-1} \Delta x_{k-1} + \bar{B}_{k-1}^- \Delta u_{k-1} \\ & + \bar{B}_{k-1}^+ \Delta u_k + \nu_{k-1}, \end{aligned} \quad (17b)$$

$$L_{g_{\text{LoS}}}^\ell(x_k, u_k) = \nu_{g_{\text{LoS}}}^\ell, \quad (17c)$$

$$x_{\min}^i \leq x_k^i \leq x_{\max}^i, \quad (17d)$$

$$u_{\min}^j \leq u_{k-1}^j \leq u_{\max}^j, \quad (17e)$$

$$x_0 = x_i, \quad x_N = x_f, \quad (17f)$$

where appropriate, $\forall i \in \{0, \dots, n_x\}, \forall j \in \{0, \dots, n_u\}, \forall k \in \{1, \dots, N\}, \forall \ell \in \{1, \dots, n_{kp}\}$.

B. Cinematography Scenario

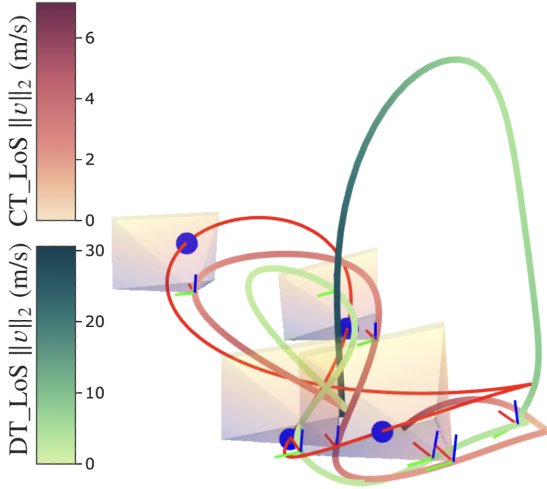
The cinematography scenario, seen in Fig. 4a, draws inspiration from the LoS guidance challenge in drone-enabled cinematography. In this scenario, a single dynamic keypoint with a known position, representing the subject to be filmed, must remain within LoS of the drone. Additionally, the drone must be within a minimum and maximum range of the subject. The subject's trajectory follows a simple sinusoidal function. A non-symmetric ℓ_∞ -norm cone is used to model the viewcone. Since the final state of the subject implicitly determines the time-of-flight (ToF) and final state constraint, the ToF is arbitrarily fixed, and there is no explicit terminal state constraint. The objective of this scenario is to minimize fuel cost, $\int_{t_0}^{t_f} \|u(t)\|_2 dt$.

C. Relative Navigation Scenario

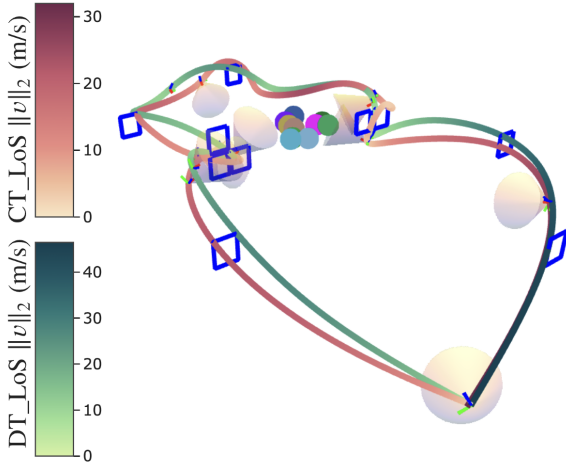
The relative navigation experiment, seen in Fig. 4b, is inspired by the LoS guidance challenge encountered in vision-aided drone racing [35]. In this scenario, ten static keypoints serve as landmarks for visual-inertial odometry and must remain within the LoS as the drone navigates through ten square gates in a predefined sequence. The goal is to complete this sequence in minimal time. The scenario is visualized in Fig. 5. A symmetric ℓ_2 -norm cone is used to model the viewcone.

D. Implementation Details

The code used to generate the results in this paper is written in Python. During the discretization step, equations (13b), (13c), and (13d) are evaluated using the 4th order Runge Kutta method from the SciPy package, [36]. The convex subproblems for both methods are solved using the package `cvxpy`, [37], [38], using the convex solver, Clarabel [39]. The Jacobians are calculated using automatic differentiation in JAX, [40]. All further implementation details as well as the code base can



(a) Cinematography: Tracking dynamics keypoints



(b) Relative Navigation: Tracking multiple static keypoints

Fig. 4: Cinematography and Relative Navigation Scenarios: The drone’s path is shown with a color gradient indicating the L_2 -norm of velocity for both the baseline and proposed methods. The keypoints are denoted by dots. The drones and keypoints pose is shown at several time points. The view cone is displayed only for the CT-LoS method at several specific points. In the cinematography scenario, the keypoints’ trajectory is shown in solid red.

be found here. The constraint violation and runtime comparisons are run on a workstation with an AMD 7950X3D CPU and 128 GB of memory.

VII. RESULTS & DISCUSSION

To address the question of LoS violation (**Q1**), the relative navigation scenario with a grid size of 33 nodes, CT-LoS achieves an average LoS_{vio} of 2.00×10^{-3} , significantly lower than DT-LoS at 1.05×10^1 , as seen in Fig. 6c. This indicates that CT-LoS maintains the LoS constraint more effectively throughout the entire trajectory. Similarly, in the cinematography scenario with a grid size of 15 nodes, CT-LoS achieves an average

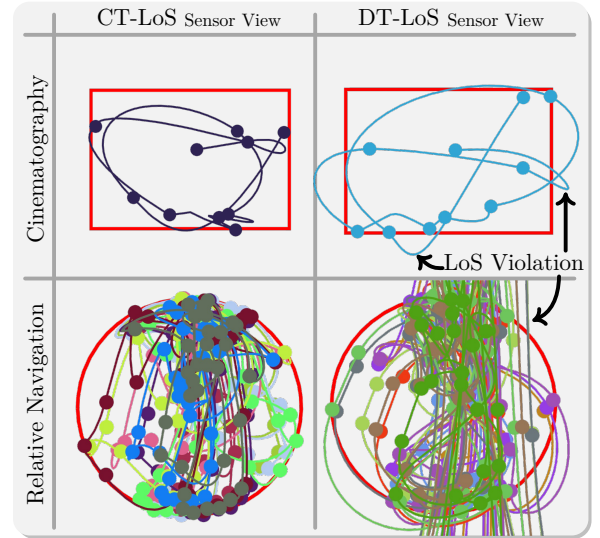


Fig. 5: Qualitative Results: The trajectories of keypoints for both CT-LoS and DT-LoS methods are displayed. Dots represent discrete nodes, while solid lines represent nonlinear keypoint paths. Different colors are used to distinguish multiple keypoint paths.

LoS_{vio} of 4.03×10^{-3} , compared to DT-LoS at 1.23, as seen in Fig.6d. These results demonstrate that CT-LoS consistently outperforms DT-LoS in maintaining LoS constraints.

Regarding the tradeoffs made to achieve better LoS violation performance (**Q2**), the primary tradeoff of the proposed approach is the potential sacrifice in objective performance. While CT-LoS penalizes the integral of LoS_{vio} along the trajectory, DT-LoS only penalizes LoS_{vio} at discrete points. This can be seen in Fig. 6d and Fig. 6c, in which the CT-LoS curve is below the DT-LoS except for large node counts in the cinematography scenario. This is expected as DT-LoS solves a less constrained approximation of the true NLP we are trying to solve. CT-LoS directly solves the true NLP by penalizing the integral of LoS_{vio} along the trajectory resulting in a more constrained problem.

Concerning the scalability of CT-LoS as the problem size increases (**Q3**), runtime for both formulations scales linearly with grid size, but DT-LoS has a steeper slope, especially in the relative navigation scenario. For example, increasing the grid size to 132 nodes improves DT-LoS LoS_{vio} to 3.14×10^{-3} , but at the cost of a prohibitively longer runtime of 3.00×10^2 seconds, compared to CT-LoS at 5.43 seconds, as seen in Fig. 6c and Fig. 6a. In the cinematography scenario, increasing the grid size to 40 nodes reduces DT-LoS LoS_{vio} to 1.15×10^{-3} , but increases runtime to 2.47 seconds, compared to CT-LoS at 8.24×10^{-1} seconds, as seen in Fig. 6d and Fig. 6b. This is due to the increased number of constraints added to the DT-LoS convex subproblem with each additional node. In contrast, CT-LoS adds only a single LICQ constraint and an additional row to the dynamics constraint per additional node, making it more computationally efficient. Furthermore, DT-LoS requires at least twice the number

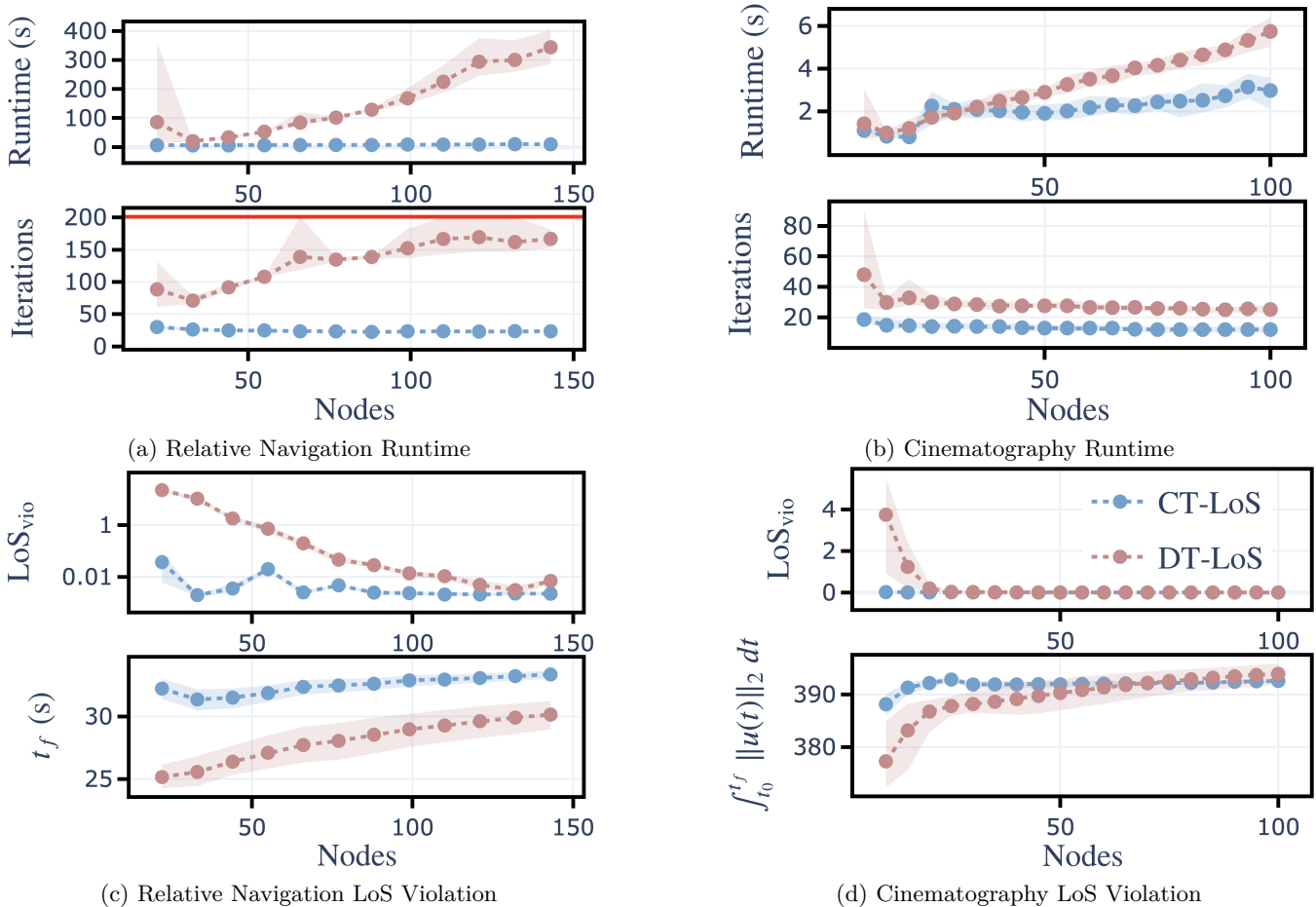


Fig. 6: Quantitative Results: (a) and (b) show the total runtime and number of iterations until convergence of Alg. 1 respectively. (c) and (d) show the LoS constraint violation and the time-of-flight or total fuel cost respectively. The shaded regions represent the minimum and maximum and the dots represent the average values of runtime and iterations for the upper and lower plots respectively. For all plots, lower is better. The maximum number of iterations is denoted by the red horizontal line in the iteration plots.

of iterations to converge compared to CT-LoS, highlighting the scalability advantage of CT-LoS as the problem size increases.

The CT-LoS algorithm demonstrates its efficacy across two challenging scenarios inspired by real-world problems. Across both scenarios, our algorithm consistently shows either lower or equivalent LoS_{vio} than DT-LoS. As the grid size increases, DT-LoS performance converges to that of CT-LoS due to more frequent enforcement of nodal LoS constraints. The CT-LoS formulation remains largely unaffected by grid size due to its integral constraint violation penalty. Notably, CT-LoS does sacrifice objective performance, which can be seen in Fig. 6d and Fig. 6c, except for larger grid sizes in the cinematography scenario.

VIII. CONCLUSION

In this work, we addressed three central challenges within the line-of-sight (LoS) guidance problem. We proposed a sensor footprint agnostic LoS constraint with a convex norm cone and nonconvex transformation components. Additionally, we developed a computationally

tractable formulation of a continuous-time LoS guidance method, CT-LoS, which leverages the CT-SCvx algorithm from [26]. We then demonstrated the proposed method’s efficacy in several representative and challenging scenarios inspired by real-world applications. Finally, we compared it against a baseline formulation. This work is a step forward to building reliable real-time planning algorithms suitable for safety-critical applications.

REFERENCES

- [1] G. Huang, “Visual-inertial navigation: A concise review,” in *2019 Int. Conf. on Robotics and Automation (ICRA)*, pp. 9572–9582, IEEE, May 2019.
- [2] D. Scaramuzza and F. Fraundorfer, “Visual odometry [tutorial],” *IEEE Robot. Autom. Mag.*, vol. 18, pp. 80–92, Dec. 2011.
- [3] C. Huang *et al.*, “ACT: An autonomous drone cinematography system for action scenes,” in *2018 IEEE Int. Conf. on Robotics and Automation (ICRA)*, pp. 7039–7046, IEEE, May 2018.
- [4] A. Alcántara, J. Capitán, R. Cunha, and A. Ollero, “Optimal trajectory planning for cinematography with multiple unmanned aerial vehicles,” *Rob. Auton. Syst.*, vol. 140, p. 103778, June 2021.
- [5] C. R. Hayner, S. C. Buckner, D. Broyles, E. Madewell, K. Leung, and B. Açikmeşe, “HALO: Hazard-aware landing optimization for autonomous systems,” in *2023 IEEE Int. Conf.*

- on *Robotics and Automation (ICRA)*, pp. 3261–3267, IEEE, May 2023.
- [6] J. M. Carson *et al.*, “The SPLICE project: Continuing NASA development of GN&C technologies for safe and precise landing,” in *AIAA Scitech 2019 Forum*, (Reston, Virginia), American Institute of Aeronautics and Astronautics, Jan. 2019.
 - [7] A. E. Johnson and J. F. Montgomery, “Overview of terrain relative navigation approaches for precise lunar landing,” in *2008 IEEE Aerospace Conf.*, pp. 1–10, IEEE, Mar. 2008.
 - [8] B. Zhou, J. Pan, F. Gao, and S. Shen, “RAPTOR: Robust and perception-aware trajectory replanning for quadrotor fast flight,” *IEEE Trans. Robot.*, vol. 37, pp. 1992–2009, Dec. 2021.
 - [9] J. Tordesillas and J. P. How, “Panther: Perception-aware trajectory planner in dynamic environments,” *IEEE Access*, vol. 10, pp. 22662–22677, 2022.
 - [10] I. Spasojevic, V. Murali, and S. Karaman, “Perception-aware time optimal path parameterization for quadrotors,” in *2020 IEEE Int. Conf. on Robotics and Automation (ICRA)*, pp. 3213–3219, IEEE, May 2020.
 - [11] V. Murali, I. Spasojevic, W. Guerra, and S. Karaman, “Perception-aware trajectory generation for aggressive quadrotor flight using differential flatness,” in *2019 American Control Conf. (ACC)*, pp. 3936–3943, IEEE, July 2019.
 - [12] D. Falanga, P. Foehn, P. Lu, and D. Scaramuzza, “PAMPC: Perception-aware model predictive control for quadrotors,” in *2018 IEEE/RSJ Int. Conf. on Intelligent Robots and Systems (IROS)*, pp. 1–8, Oct. 2018.
 - [13] T. P. Reynolds, M. Szmuk, D. Malyuta, M. Mesbahi, B. Açıkmeşe, and J. M. Carson, “Dual quaternion-based powered descent guidance with state-triggered constraints,” *Journal of Guidance, Control, and Dynamics*, vol. 43, no. 9, pp. 1584–1599, 2020.
 - [14] M. Kelly, “An introduction to trajectory optimization: How to do your own direct collocation,” *SIAM Rev. Soc. Ind. Appl. Math.*, vol. 59, pp. 849–904, Jan. 2017.
 - [15] D. Mellinger and V. Kumar, “Minimum snap trajectory generation and control for quadrotors,” in *2011 IEEE Int. Conf. on Robotics and Automation*, pp. 2520–2525, May 2011.
 - [16] C. Richter, A. Bry, and N. Roy, “Polynomial trajectory planning for aggressive quadrotor flight in dense indoor environments,” in *Robotics Research: The 16th Int. Symposium ISRR* (M. Inaba and P. Corke, eds.), pp. 649–666, Cham: Springer Int. Publishing, 2016.
 - [17] W. Ding, W. Gao, K. Wang, and S. Shen, “An efficient B-spline-based kinodynamic replanning framework for quadrotors,” *IEEE Trans. Rob.*, vol. 35, pp. 1287–1306, Dec. 2019.
 - [18] B. Houska, H. J. Ferreau, and M. Diehl, “ACADO toolkit—an open-source framework for automatic control and dynamic optimization,” *Optim. Control Appl. Methods*, vol. 32, pp. 298–312, May 2011.
 - [19] S. G. Johnson, “The NLOpt nonlinear-optimization package.”
 - [20] A. Wächter and L. T. Biegler, “On the implementation of an interior-point filter line-search algorithm for large-scale nonlinear programming,” *Math. Program.*, vol. 106, pp. 25–57, Mar. 2006.
 - [21] P. T. Boggs and J. W. Tolle, “Sequential quadratic programming,” *Acta Numer.*, vol. 4, pp. 1–51, Jan. 1995.
 - [22] D. Malyuta *et al.*, “Convex optimization for trajectory generation: A tutorial on generating dynamically feasible trajectories reliably and efficiently,” *IEEE Control Systems Magazine*, vol. 42, no. 5, pp. 40–113, 2022.
 - [23] Y. Mao, D. Dueri, M. Szmuk, and B. Açıkmeşe, “Successive convexification of non-convex optimal control problems with state constraints,” *IFAC-PapersOnLine*, vol. 50, pp. 4063–4069, July 2017.
 - [24] R. Bonalli, A. Cauligi, A. Bylard, and M. Pavone, “GuSTO: Guaranteed sequential trajectory optimization via sequential convex programming,” in *2019 Int. Conf. on Robotics and Automation (ICRA)*, pp. 6741–6747, IEEE, May 2019.
 - [25] Y. Yu, P. Elango, U. Topcu, and B. Açıkmeşe, “Proportional–integral projected gradient method for conic optimization,” *Automatica*, vol. 142, p. 110359, Aug. 2022.
 - [26] P. Elango, D. Luo, A. G. Kamath, S. Uzun, T. Kim, and B. Açıkmeşe, “Successive convexification for trajectory optimization with Continuous-Time constraint satisfaction,” Apr. 2024.
 - [27] M. Szmuk, *Successive Convexification & High Performance Feedback Control for Agile Flight*. PhD thesis, University of Washington, June 2019.
 - [28] M. Jacquet and A. Franchi, “Enforcing vision-based localization using perception constrained n-mpc for multi-rotor aerial vehicles,” in *2022 IEEE/RSJ Int. Conf. on Intelligent Robots and Systems (IROS)*, pp. 1818–1824, 2022.
 - [29] M. Szmuk and B. Açıkmeşe, “Successive convexification for 6-DoF mars rocket powered landing with Free-Final-Time,” Feb. 2018.
 - [30] S. Boyd and L. Vandenberghe, *Convex Optimization*. Cambridge, England: Cambridge University Press, Mar. 2004.
 - [31] A. G. Kamath *et al.*, “Real-Time sequential conic optimization for Multi-Phase rocket landing guidance,” *IFAC-PapersOnLine*, vol. 56, pp. 3118–3125, Jan. 2023.
 - [32] P. J. Antsaklis and A. N. Michel, *Linear systems*. Secaucus, NJ: Birkhauser Boston, 1 ed., Oct. 2005.
 - [33] T. Reynolds, D. Malyuta, M. Mesbahi, B. Açıkmeşe, and J. M. Carson, “A Real-Time algorithm for Non-Convex powered descent guidance,” in *AIAA Scitech 2020 Forum*, AIAA SciTech Forum, American Institute of Aeronautics and Astronautics, Jan. 2020.
 - [34] D. Drusvyatskiy and A. S. Lewis, “Error bounds, quadratic growth, and linear convergence of proximal methods,” *Math. Oper. Res.*, vol. 43, pp. 919–948, Aug. 2018.
 - [35] Y. Song, A. Romero, M. Müller, V. Koltun, and D. Scaramuzza, “Reaching the limit in autonomous racing: Optimal control versus reinforcement learning,” *Sci Robot*, vol. 8, p. eadg1462, Sept. 2023.
 - [36] P. Virtanen *et al.*, “SciPy 1.0: Fundamental Algorithms for Scientific Computing in Python,” *Nature Methods*, vol. 17, pp. 261–272, 2020.
 - [37] A. Agrawal, R. Verschueren, S. Diamond, and S. Boyd, “A rewriting system for convex optimization problems,” *Journal of Control and Decision*, vol. 5, no. 1, pp. 42–60, 2018.
 - [38] S. Diamond and S. Boyd, “CVXPY: A Python-embedded modeling language for convex optimization,” *Journal of Machine Learning Research*, vol. 17, no. 83, pp. 1–5, 2016.
 - [39] P. J. Goulart and Y. Chen, “Clarabel: An interior-point solver for conic programs with quadratic objectives,” *arXiv [math.OA]*, May 2024.
 - [40] J. Bradbury *et al.*, “JAX: composable transformations of Python+NumPy programs,” 2018.